Structured Input-Output Analysis of Oblique Laminar-Turbulent Patterns in plane Couette-Poiseuille Flow*

Yu Shuai[a,*], Chang Liu[b], Dennice F. Gayme[c]

[a] *Department of Mechanical and Aerospace Engineering, Princeton University, Princeton, 08544, New Jersey, United States*
[b] *Department of Physics, University of California, Berkeley, Berkeley, 94720, California, United States*
[c] *Department of Mechanical Engineering, Johns Hopkins University, Baltimore, 21218, Maryland, United States*

Abstract

In this work, we employ structured input-output analysis to study the flow patterns in transitional plane Couette-Poiseuille flow (CPF). First, we focus on the well-studied intermediate laminar profile, which balances the shear and pressure effects. We show that the highest structured gain corresponds to perturbations with wavelengths associated with the oblique turbulent bands observed in experiments. In addition, the inclination angles of these structures show a Reynolds number dependence consistent with experimentally observed trends. We then examine the Reynolds number scaling of the maximal structured frequency response as the velocity profile varies from plane Couette to Poiseuille flow. Our results demonstrate that, as expected, the scaling exponent increases over this range, but this increase is not monotonic. We attribute this scaling variation to the change in flow patterns that dominate each flow regime. We then focus on the particular case of plane Couette flow and compute the structured response modes. Their behavior and structural features are consistent with results obtained through direct numerical

*This document is the results of the research project funded by the National Science Foundation.

*Corresponding author
E-mail address: yu_shuai@princeton.edu (Y. Shuai), chang_liu@berkeley.edu (C. Liu), and dennice@jhu.edu (D. F. Gayme)

simulation (DNS) studies. Finally, we employ the structured analysis framework to examine the temporal evolution of the dominant structures. For the well-studied cases of plane Couette and plane Poiseuille flows, the computed advection speeds of the oblique structures are consistent with those predicted through DNS.

Keywords: Structured Input-Output Analysis, Laminar-Turbulent Patterns, Couette-Poiseuille Flow

1. Introduction

A coexistence of turbulent and laminar behavior has been observed in wall-bounded shear flows as they transition from a laminar to a turbulent regime [Tuckerman et al., 2020]. Previous studies have shown that this transitional state usually takes the form of banded laminar and turbulent regions with an oblique angle relative to the streamwise direction [Prigent et al., 2003, Kanazawa, 2018]. Numerical simulations [Tuckerman and Barkley, 2011, Tuckerman et al., 2014, Fukudome and Iida, 2012] and experiments [Prigent et al., 2003] have indicated that both the wavelengths and inclination angles of these structures depend on the Reynolds number. These structures have also been used as initial conditions to induce turbulence in direct numerical simulations (DNS) [Tao et al., 2018].

While the prevalence and large amplification of oblique turbulent bands in transitional wall-bounded shear flows has been widely observed, a comprehensive understanding of their underlying dynamics and role in transition has yet to be realized. The large channel sizes ($\sim O(100)$ channel half-heights), which is required to observe such patterns, complicates the study of these structures, see e.g., [Prigent et al., 2002, Tuckerman and Barkley, 2011, Kim et al., 2020]. Computations of exact coherent structures in channel flows also highlight the large domain sizes required to characterize the laminar-turbulent interface of these flow patterns [Schneider et al., 2010]. These large channel extents increase the computational costs of DNS and the complexity of experiments that are needed to study these structures further.

The recently introduced structured input-output analysis has been shown to predict large amplification of oblique structures in transitional plane Couette flow (PCF) and plane Poiseuille flow (PPF) [Liu and Gayme, 2021] at a similar computational cost to traditional input-output analysis. Structured input-output analysis builds upon traditional approaches that analyze

the spatiotemporal frequency response of the linearized Navier-Stokes (LNS) equations, see, e.g., Bamieh and Dahleh [2001], Jovanović and Bamieh [2005], through the addition of a feedback loop with a structured model of the nonlinear interactions. Analysis of this feedback interconnection predicts maximally amplified structures with features consistent with nonlinear optimal perturbations [Rabin et al., 2012, Farano et al., 2015] and DNS studies [Reddy et al., 1998, Tuckerman et al., 2020]. It also identifies the oblique turbulent bands observed in experiments [Prigent et al., 2003] and DNS [Kanazawa, 2018] of channel flows, as well as those seen in both stratified [Liu et al., 2022] and rotating plane Couette flow [Liu, 2021].

This work builds on the study of Shuai et al. [2022], which uses structured input-output analysis to analyze transitional plane Couette-Poiseuille flows (CPF). In this flow configuration, the laminar base flow is parameterized by $\eta \in [-1, 1]$ to adjust the ratio of background shear to pressure driving. Plane Couette flow and Poiseuille flow correspond to the two extremes of the parameter range, respectively $\eta = -1$ and $\eta = 1$. We first focus on the widely studied intermediate case ($\eta = 0$) in which the shear and pressure gradient forcing are equally weighted [Klotz and Wesfreid, 2017, Klotz et al., 2021, Liu et al., 2021]. Our results indicate that the oblique laminar-turbulent patterns with nonzero streamwise and spanwise wavenumbers show the highest structured gain. The associated wavenumber ranges of the predicted oblique turbulent bands are consistent with recent experimental observations [Klotz et al., 2021]. In addition, the wavenumbers and inclination angles associated with the highest structured gain vary as a function of Reynolds number, which is consistent with trends observed in related wall-bounded shear flows, see, e.g., Prigent et al. [2003].

We obtain the scaling of the highest structured gain for this intermediate base flow as $\sim O(Re^{\alpha})$ with $\alpha = 1.3$, which is halfway between the respective values of $\alpha = 1.1$ for plane Couette flow and 1.5 for plane Poiseuille [Liu and Gayme, 2021]. However, the increase in the exponent as the flow smoothly transitions from purely shear (plane Couette flow) to purely pressure driving (plane Poiseuille flow) is not monotonic. Our analysis indicates that changes in the slope of the curve correspond to changes in the most amplified flow structures, i.e., the emergence of different optimal perturbation structures.

We further study the structural features of the oblique turbulent bands by computing the response modes associated with the optimal perturbations for the particular case of plane Couette flow. The resulting wall-normal profiles and velocity field are consistent with previous numerical results [Xiao and

Song, 2020b, Chantry et al., 2016].

In the last section of the paper, we describe how the structured input-output analysis framework can be adapted to estimate the downstream advection speed of structures associated with a particular spatio-temporal wavenumber triplet. The advection speeds of the oblique turbulent bands predicted through these computations compare favorably to measurements based on DNS of plane Couette and plane Poiseuille flows [Xiao and Song, 2020a, Tuckerman et al., 2014, Lu et al., 2019, Fukudome and Iida, 2012]. We then apply this computation to numerically evaluate the dependence of the structured frequency response on the phase speed.

We organize the remainder of this paper as follows. In section 2, we introduce the plane Couette-Poiseuille flow equations and describe the procedure for computing the structured input-output gain for this system. We then compute the structured response for the intermediate CPF profile and compare its behavior to results from traditional input-output analysis in section 3. The Reynolds number scaling and types of structures with the highest response as the flow transitions from plane Couette to plane Poiseuille flow are evaluated and discussed in section 4. In section 5 we provide a method for computing the structured modes, which we use to study the wall-normal variation and velocity field associated with the oblique waves for the particular case of plane Couette flow. We then describe how to use the structured input-output approach to estimate the advection speed of spatial structures in section 6. The paper concludes in section 7, where we summarize the results and outline further research directions.

2. Structured input-output analysis formulation

We consider incompressible flow between two infinite parallel plates with streamwise, wall-normal, spanwise, and time coordinates (x, y, z, t), respectively. The total velocity is decomposed into a laminar base flow and fluctuations about that base flow, i.e., $\boldsymbol{u}_{tot} = [U(y), 0, 0]^{\mathrm{T}} + \boldsymbol{u}$. The pressure is similarly decomposed as $p_{tot} = P + p$. We employ the laminar base flow from Klotz and Wesfreid [2017], which is given by

$$U(y) = \frac{3(1+\eta)}{4}(y^2 - 1) + \frac{1-\eta}{2}(y-1) + 1. \tag{1}$$

The parameter $\eta \in [-1, 1]$ determines the relative contribution of shear versus pressure gradient with $\eta = -1$ corresponding to plane Couette flow with

laminar profile $U(y) = y$, and $\eta = 1$ corresponding to plane Poiseuille flow with laminar profile $U(y) = 1.5y^2 - 0.5$. Here, the streamwise velocity is normalized by the upper-plate speed U^* corresponding to the flow regime that is purely plane Couette flow. The length is normalized by the channel half-height h, leading to a wall-normal domain of $y \in [-1, 1]$. The Reynolds number is defined as $Re := \frac{U^* h}{\nu}$, where ν denotes the kinematic viscosity.

The dynamics of the velocity fluctuations $\boldsymbol{u} := [u,\, v,\, w]^{\mathrm{T}}$ are governed by the Navier-Stokes equations (NSE). Following Liu and Gayme [2021], we decompose the NSE into the linearized dynamics about the laminar base flow plus nonlinear terms, which are treated as forcing $\boldsymbol{f} := -\boldsymbol{u} \cdot \boldsymbol{\nabla} \boldsymbol{u} = [f_x, f_y, f_z]^{\mathrm{T}}$. We then replace this nonlinearity with the following input-output model

$$\boldsymbol{f}_\xi := \begin{bmatrix} -\boldsymbol{u}_\xi^{\mathrm{T}} & & \\ & -\boldsymbol{u}_\xi^{\mathrm{T}} & \\ & & -\boldsymbol{u}_\xi^{\mathrm{T}} \end{bmatrix} \begin{bmatrix} \boldsymbol{\nabla} u \\ \boldsymbol{\nabla} v \\ \boldsymbol{\nabla} w \end{bmatrix} = \begin{bmatrix} f_{x,\xi} \\ f_{y,\xi} \\ f_{z,\xi} \end{bmatrix}, \tag{2}$$

where $\boldsymbol{u}_\xi$ represents an input-output gain from the modeled forcing $\boldsymbol{f}_\xi$ to the velocity gradient $\boldsymbol{\nabla} \boldsymbol{u}$. Writing the nonlinearity in terms of this gain operator allows the model to remain linear in the velocity, thereby simplifying the representation and analysis. Although the model has a simplified representation, it preserves the componentwise structure of the nonlinear interactions of the NSE since all elements outside of the block-diagonal elements $\boldsymbol{u}_\Xi := \mathrm{diag}(-\boldsymbol{u}_\xi^{\mathrm{T}}, -\boldsymbol{u}_\xi^{\mathrm{T}}, -\boldsymbol{u}_\xi^{\mathrm{T}})$ are zero.

We employ the standard transformation to write the governing equations in terms of the fluctuating wall-normal velocity and vorticity $[v,\, \omega_y]^T$. We then perform the triple Fourier transform

$$\widehat{(\cdot)}(y; k_x, k_z, \omega) := \int_{-\infty}^{\infty} \int_{-\infty}^{\infty} \int_{-\infty}^{\infty} (\cdot)(x, y, z, t) e^{-\mathrm{i}(k_x x + k_z z + \omega t)} dx dz dt. \tag{3}$$

Here k_x and k_z are the respective streamwise and spanwise wavenumbers, ω is the temporal frequency, and $\mathrm{i} = \sqrt{-1}$. The transformed linearized NSE driven by the modeled forcing $\widehat{\boldsymbol{f}}_\xi = [\widehat{f}_{x,\xi}, \widehat{f}_{y,\xi}, \widehat{f}_{z,\xi}]^{\mathrm{T}}$ for each (k_x, k_z, ω) triplet is then given by

$$\mathrm{i}\omega \begin{bmatrix} \widehat{v} \\ \widehat{\omega}_y \end{bmatrix} = \widehat{\mathcal{A}} \begin{bmatrix} \widehat{v} \\ \widehat{\omega}_y \end{bmatrix} + \widehat{\mathcal{B}} \begin{bmatrix} \widehat{f}_{x,\xi} \\ \widehat{f}_{y,\xi} \\ \widehat{f}_{z,\xi} \end{bmatrix}, \tag{4a}$$

$$\begin{bmatrix} \widehat{u} \\ \widehat{v} \\ \widehat{w} \end{bmatrix} = \widehat{\mathcal{C}} \begin{bmatrix} \widehat{v} \\ \widehat{\omega}_y \end{bmatrix}, \tag{4b}$$

where the operators $\widehat{\mathcal{A}}$, $\widehat{\mathcal{B}}$ and $\widehat{\mathcal{C}}$ are defined following [Jovanović and Bamieh, 2005] as

$$\widehat{\mathcal{A}} := \mathcal{M}^{-1} \begin{bmatrix} -\mathrm{i}k_x U \widehat{\nabla}^2 + \mathrm{i}k_x U'' + \widehat{\nabla}^4/Re & 0 \\ -\mathrm{i}k_z U' & -\mathrm{i}k_x U + \widehat{\nabla}^2/Re \end{bmatrix}, \tag{5a}$$

$$\widehat{\mathcal{B}} := \mathcal{M}^{-1} \begin{bmatrix} -\mathrm{i}k_x \partial_y & -(k_x^2 + k_z^2) & -\mathrm{i}k_z \partial_y \\ \mathrm{i}k_z & 0 & -\mathrm{i}k_x \end{bmatrix}, \quad \mathcal{M} := \begin{bmatrix} \widehat{\nabla}^2 & 0 \\ 0 & 1 \end{bmatrix}, \tag{5b}$$

$$\widehat{\mathcal{C}} := \frac{1}{k_x^2 + k_z^2} \begin{bmatrix} \mathrm{i}k_x \partial_y & -\mathrm{i}k_z \\ k_x^2 + k_z^2 & 0 \\ \mathrm{i}k_z \partial_y & \mathrm{i}k_x \end{bmatrix}. \tag{5c}$$

No-penetration and no-slip boundary conditions $\widehat{v}(y = \pm 1) = \partial \widehat{v}/\partial y\,(y = \pm 1) = \widehat{\omega}_y(y = \pm 1) = 0$ are employed. The spatio-temporal frequency response operator mapping the modeled input forcing $\widehat{\boldsymbol{f}}_\xi(y; k_x, k_z, \omega)$ to the velocity fluctuations $\widehat{\boldsymbol{u}}(y; k_x, k_z, \omega)$ is

$$\mathcal{H}(y; k_x, k_z, \omega) := \widehat{\mathcal{C}}(\mathrm{i}\omega \mathbb{I} - \widehat{\mathcal{A}})^{-1} \widehat{\mathcal{B}}, \tag{6}$$

where $\mathbb{I}$ is the identity operator.

In order to compute the structured response, we must first combine the modeled nonlinearity with the spatio-temporal frequency response. We accomplish this by first defining a modified response operator [Liu and Gayme, 2021]

$$\mathcal{H}_\nabla(y; k_x, k_z, \omega) := \mathrm{diag}(\widehat{\boldsymbol{\nabla}}, \widehat{\boldsymbol{\nabla}}, \widehat{\boldsymbol{\nabla}}) \mathcal{H}(y; k_x, k_z, \omega). \tag{7}$$

This modification leads results in different output, $\widehat{\boldsymbol{\nabla}} \widehat{\boldsymbol{u}}$, but enables us to isolate the expression $\widehat{\boldsymbol{u}}_\Xi$, which represents the input-output gain for the model of the nonlinearity in (2). More specifically, the reformulated system, shown in Fig. 1, is defined in terms of the feedback interconnection between $\mathcal{H}_\nabla$ and the block-diagonal structured gain $\widehat{\boldsymbol{u}}_\Xi := \mathrm{diag}(-\widehat{\boldsymbol{u}}_\xi^{\mathrm{T}}, -\widehat{\boldsymbol{u}}_\xi^{\mathrm{T}}, -\widehat{\boldsymbol{u}}_\xi^{\mathrm{T}})$. The output

$$\widehat{\boldsymbol{\nabla}} \widehat{\boldsymbol{u}} = \mathcal{H}_\nabla \widehat{\boldsymbol{f}}_\xi \tag{8}$$

is the 9-by-1 vectorized velocity gradient $\widehat{\boldsymbol{\nabla}} \widehat{\boldsymbol{u}} := [(\widehat{\boldsymbol{\nabla}} \widehat{u})^{\mathrm{T}}, (\widehat{\boldsymbol{\nabla}} \widehat{v})^{\mathrm{T}}, (\widehat{\boldsymbol{\nabla}} \widehat{w})^{\mathrm{T}}]^{\mathrm{T}}$.

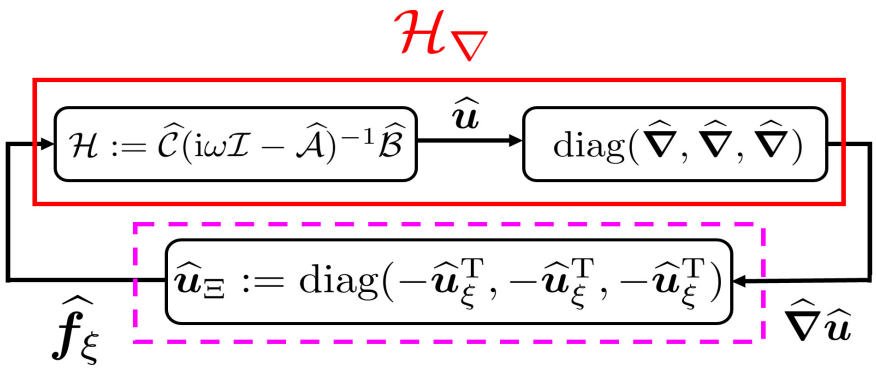

Figure 1: Illustration of the structured feedback interconnection between the modified frequency response operator $\mathcal{H}_\nabla := \mathrm{diag}(\widehat{\boldsymbol{\nabla}}, \widehat{\boldsymbol{\nabla}}, \widehat{\boldsymbol{\nabla}})\mathcal{H}$ (comprising blocks inside the red solid line —) and the structured uncertainty $\widehat{\boldsymbol{u}}_\Xi := \mathrm{diag}(-\widehat{\boldsymbol{u}}_\xi^{\mathrm{T}}, -\widehat{\boldsymbol{u}}_\xi^{\mathrm{T}}, -\widehat{\boldsymbol{u}}_\xi^{\mathrm{T}})$ (the block inside the purple dashed line - - -). The modeled forcing term $\widehat{\boldsymbol{f}}_\xi := [\widehat{f}_{x,\xi}, \widehat{f}_{y,\xi}, \widehat{f}_{z,\xi}]^{\mathrm{T}} := \widehat{\boldsymbol{u}}_\Xi\widehat{\boldsymbol{\nabla}}\widehat{\boldsymbol{u}}$, where $\widehat{\boldsymbol{\nabla}}\widehat{\boldsymbol{u}} := [(\widehat{\boldsymbol{\nabla}}\widehat{u})^{\mathrm{T}}, (\widehat{\boldsymbol{\nabla}}\widehat{v})^{\mathrm{T}}, (\widehat{\boldsymbol{\nabla}}\widehat{w})^{\mathrm{T}}]^{\mathrm{T}}$ is the 9-by-1 vectorized velocity gradient.

We then define the structured input-output response [Liu and Gayme, 2021] as

$$\|\mathcal{H}_\nabla\|_\mu(k_x, k_z) := \sup_{\omega\in\mathbb{R}} \mu_{\widehat{\boldsymbol{U}}_\Xi}\left[\mathbf{H}_\nabla(k_x, k_z, \omega)\right], \tag{9}$$

where

$$\mu_{\widehat{\boldsymbol{U}}_\Xi}\left[\mathbf{H}_\nabla\right] := \begin{cases} 1/\min\{\bar{\sigma}\left[\widehat{\boldsymbol{u}}_\Xi\right] : \widehat{\boldsymbol{u}}_\Xi \in \widehat{\boldsymbol{U}}_\Xi, \det\left[\mathbb{I} - \mathbf{H}_\nabla\widehat{\boldsymbol{u}}_\Xi\right] = 0\}, \\ \\ 0, \text{if } \forall\ \widehat{\boldsymbol{u}}_\Xi \in \widehat{\boldsymbol{U}}_\Xi, \det\left[\mathbb{I} - \mathbf{H}_\nabla\widehat{\boldsymbol{u}}_\Xi\right] \neq 0 \end{cases} \tag{10}$$

is the structured singular value of $\mathbf{H}_\nabla(k_x, k_z, \omega)$ for each triplet (k_x, k_z, ω) associated with structured uncertainty set $\widehat{\boldsymbol{U}}_\Xi$ [Packard and Doyle, 1993]. Here the symbol $\bar{\sigma}[\cdot]$ represents the largest singular value of the argument, $\det[\cdot]$ is the determinant of the argument, and $\mathbf{H}_\nabla$ denotes the discretized spatiotemporal frequency response operator computed based on the discretization of the operators in (10) along the wall-normal direction. The subscript of μ in eq.(9), i.e., $\widehat{\boldsymbol{U}}_\Xi := \{\mathrm{diag}(-\widehat{\mathbf{u}}_\xi^{\mathrm{T}}, -\widehat{\mathbf{u}}_\xi^{\mathrm{T}}, -\widehat{\mathbf{u}}_\xi^{\mathrm{T}}) : -\widehat{\mathbf{u}}_\xi^{\mathrm{T}} \in \mathbb{C}^{N_y\times 3N_y}\}$, is the set of wall-normally discretized structured uncertainties with the same block-diagonal structure as $\widehat{\boldsymbol{u}}_\Xi$, and N_y denotes the number collocation points excluding boundary points. From the definition above, the structured singular value can be interpreted as the maximum perturbation that the feedback interconnection in Fig. 1 can withstand while maintaining stability in the sense

defined by the small gain theorem Zhou et al. [1996], which is provided in Appendix A. Further discussion regarding the definition and interpretation of the structured response for wall-bounded shear flows can be found in Liu and Gayme [2021].

This work uses the Chebyshev collocation method [Weideman and Reddy, 2000] with $N_y = 30$ collocation points in the wall-normal direction. We use 50×90 logarithmically spaced points in the spatial wavenumber domain $k_x \in [10^{-4}, 10^{0.48}]$ and $k_z \in [10^{-2}, 10^{1.2}]$. This configuration matches that in Liu and Gayme [2021], who found this number of points sufficient for convergence of the results.

The accurate computation of structured singular values μ is NP hard, see, e.g., Packard et al. [1988], Young and Doyle [1990], and thus computationally expensive. Therefore, we instead compute an upper bound of the response in (9) using the *mussv* command in MATLAB. The current version of this toolbox does not enable us to impose the condition $\widehat{\boldsymbol{u}}_\Xi := \mathrm{diag}(-\widehat{\boldsymbol{u}}_\xi^{\mathrm{T}}, -\widehat{\boldsymbol{u}}_\xi^{\mathrm{T}}, -\widehat{\boldsymbol{u}}_\xi^{\mathrm{T}})$, wherein the three diagonal blocks are identical (i.e., there is a repeated block structure). We instead relax this constraint and compute eq.(10) while enforcing only a block diagonal structure, i.e., we allow three different values of $-\widehat{\boldsymbol{u}}_\xi^{\mathrm{T}}$. This relaxation was previously used in Liu and Gayme [2021], where the structures that were predicted most likely to induce transition were consistent with experiments of [Prigent et al., 2003], DNS [Reddy et al., 1998] and NLOP [Rabin et al., 2012, Farano et al., 2015] for both plane Couette and Poiseuille flow. Predictions that were similarly consistent with nonlinear analysis were seen in the analysis of stratified plane Couette flow in Liu et al. [2022]. Recent work in Mushtaq et al. [2022] provides algorithms for computing lower and upper bounds on the structured singular value for systems with repeated blocks. However, these iterative algorithms substantially increase the computational cost. Implementing these method and examining the trade-off between the efficiency and accuracy of algorithms for computing structured singular values for wall-bounded shear flows is a direction of ongoing work.

3. Structured frequency response

In this section, we use the method described in the previous section to analyze transitional structures in Couette-Poiseuille flow for the intermediate case $\eta = 0$, where the laminar profile (1) has an equal weighting of the contributions from plane Couette and plane Poiseuille flow. This profile is

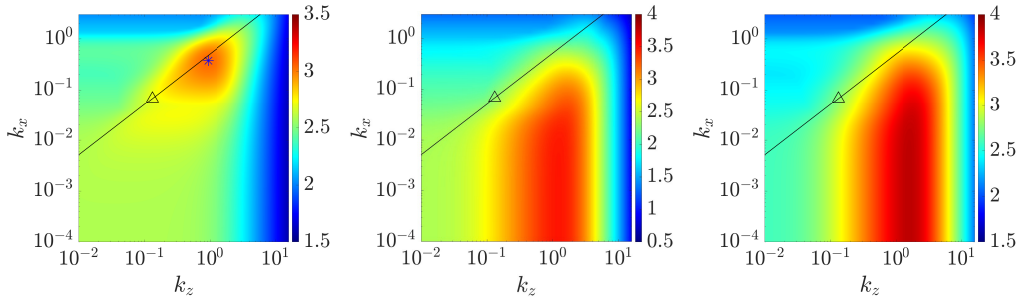

Figure 2: Contour plots of (a) $\log_{10}[\|\mathcal{H}_\nabla\|_\mu(k_x,k_z)]$, (b) $\log_{10}[\|\mathcal{H}\|_\infty(k_x,k_z)]$ and (c) $\log_{10}[\|\mathcal{H}_\nabla\|_\infty(k_x,k_z)]$ for plane Couette-Poiseuille flow $U(y)=\frac{3}{4}(y^2-1)+\frac{1}{2}(y+1)$ at $Re=610$ and $\eta=0$ in (1). Here, the black triangle (Δ) marks $\lambda_x\approx 93$ and $\lambda_z\approx 48$ which are the wavelengths of the observed oblique turbulent band at $Re=610$ [Klotz et al., 2021]. The blue asterisk ($*$) in (a) represents the wavelengths $(\lambda_x,\lambda_z)=(16.72,6.79)$ associated with the highest structured response $\|\mathcal{H}_\nabla\|_\mu$. The black solid line (-) $\lambda_z=\lambda_x\tan(27^\circ)$ corresponds to a 27° oblique angle of the oblique turbulent band.

linearly stable for all Reynolds numbers [Balakumar, 1997]. We compare our results to two similar quantities that would be obtained through traditional (unstructured) input-output analysis. The first is the worst-case amplification of velocity fluctuations over harmonic input forcing, which is represented by the maximal gain of the frequency response operator $\mathcal{H}$ over all temporal frequencies and computed as

$$\|\mathcal{H}\|_\infty(k_x,k_z):=\sup_{\omega\in\mathbb{R}}\bar{\sigma}\left[\mathbf{H}(k_x,k_z,\omega)\right]. \tag{11}$$

We also compute the unstructured amplification of the modified frequency response operator

$$\|\mathcal{H}_\nabla\|_\infty(k_x,k_z):=\sup_{\omega\in\mathbb{R}}\bar{\sigma}\left[\mathbf{H}_\nabla(k_x,k_z,\omega)\right]. \tag{12}$$

Neither of the quantities in eq.(11) and (12) include the model of the nonlinearity (i.e., do not impose any structure on the forcing for the input-output response). Comparing $\|\mathcal{H}_\nabla\|_\mu$ and $\|\mathcal{H}_\nabla\|_\infty$ enables us to isolate the effect of the block-diagonal structure imposed in the nonlinearity versus that of the modified frequency response operator, i.e., to investigate the effect of structured uncertainty in the closed loop (see Fig. 1).

Fig. 2(a) shows $\|\mathcal{H}_\nabla\|_\mu(k_x,k_z)$ at $Re=610$, which was selected to match that in Klotz et al. [2021]. The peak region of the structured frequency

response $\|\mathcal{H}_\nabla\|_\mu(k_x, k_z)$ is centered at $(\lambda_x, \lambda_z) = (16.72, 6.79)$, see the blue asterisk in the figure. The wavelengths $\lambda_x \approx 93 \pm 5$ and $\lambda_z \approx 48 \pm 5$ (the black triangles (Δ) in all panels of Fig. 2) corresponding to the oblique turbulent bands observed in Fig. 20 of Klotz et al. [2021] lie just outside the peak region and are about six times larger than the peak of the structured response. This agreement, while not perfect suggests an improvement in the predictions of the structured response over the traditional linear input-output approach. In particular, the structured approach captures the streamwise variation of these structures and their aspect ratio. Given that our method models, rather than resolves, the nonlinear interactions, exact agreement is not expected. The benefit of the structured method is its success in capturing the fact that oblique flow patterns (i.e., k_x far away from 0) rather than streamwise constant ones (i.e., $k_x \simeq 0$) are associated with the dominant response, at a reduced computational cost compared to DNS. The shape of the peak region in Fig. 2(a) also reflects the same inclination angle as the experimentally observed band $\theta := \tan^{-1}(\lambda_z/\lambda_x) = \tan^{-1}(48/93) \approx 27^\circ$ (the black solid line in Fig. 2). This favorable comparison of our results with the literature shows that structured input-output analysis captures the critical features and inclination angles of the dominant flow structures for this intermediate case of plane CPF.

Fig. 2(b) and (c) provide the respective plots of $\|\mathcal{H}\|_\infty$ and $\|\mathcal{H}_\nabla\|_\infty$ for the same Reynolds number and flow configuration. Compared with the structured approach, these unstructured responses place more emphasis on the streamwise elongated structures, which are associated with a completely different range of the streamwise wavenumber $k_x \approx 0$. These results also indicate that the change in the response is due to the structured feedback interconnection rather than the modified frequency response operator. These differences between the structured and the traditional unstructured input-output response are similar to those seen in previous studies of plane Couette and plane Poiseuille flow, where the change in the structures obtained under the structured feedback interconnection was related to a weakening of the lift-up mechanism [Liu and Gayme, 2021] that dominates the unstructured response.

We next study how the structured frequency response for the Couette-Poiseuille flow with $\eta = 0$ varies with the Reynolds number. Fig. 3(a) and (b) depict $\|\mathcal{H}_\nabla\|_\mu$ at $Re = 2000$ and 20000, respectively. These plots indicate that as the Reynolds number increases, the region of peak frequency response dilates and shifts towards larger streamwise and spanwise wave-

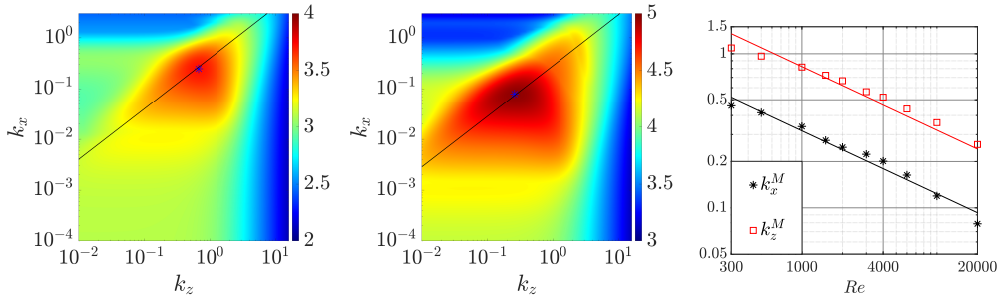

(a) (b) (c)

Figure 3: (a-b) Contour plots showing the relative location of regions associated with peak structured frequency response at (a) $Re = 2000$ and (b) 20000 with $\eta = 0$. The blue asterisks (✳) in panels (a) and (b) indicate the wavenumber pairs $(k_x^M, k_z^M) = (0.25, 0.67)$ and $(k_x^M, k_z^M) = (0.08, 0.29)$ corresponding to the highest structured frequency response $\|\mathcal{H}_\nabla\|_\mu^M$ at respective Reynolds numbers. The black solid line (—) represents $\lambda_z = \lambda_x \tan(22°)$ in panel (a) and $\lambda_z = \lambda_x \tan(15°)$ in (b) respectively, which corresponds to the inclination angle of these structures. (c) The wavenumbers corresponding to the highest structured response as a function of Reynolds number $Re \in [300, 20000]$, with corresponding scalings $k_x^M \sim Re^{-0.41}$ and $k_z^M \sim Re^{-0.34}$ shown with black and red solid lines respectively.

lengths (smaller wavenumbers). We further investigate how the peak location varies with Reynolds number by first denoting the wavenumbers of the largest structured response as k_x^M and k_z^M, which are computed as

$$(k_x^M, k_z^M) := \arg\max_{k_x, k_z} \|\mathcal{H}_\nabla\|_\mu(k_x, k_z). \tag{13}$$

This leads to $(k_x^M, k_z^M) = (0.25, 0.67)$ at $Re = 2000$ and $(k_x^M, k_z^M) = (0.08, 0.29)$ at $Re = 20000$; the values for the full range of Reynolds number $Re \in [300, 20000]$ is provided in Fig. 3(c). We then compute the ratio k_x^M/k_z^M and find that it decreases as Re increases, which indicates a reduction in the inclination angle $\theta := \tan^{-1}(k_x^M/k_z^M)$ associated with the corresponding dominant flow patterns from approximately 28° to 15° over the Reynolds number range shown.

In particular, the angles of $\theta = 22°$ and $\theta = 15°$, respectively corresponding to $Re = 2000$ and $Re = 20000$ are both lower than the inclination angle of 27° at $Re = 610$ as shown in Fig. 2(a). This decreasing trend is consistent with previous studies of laminar-turbulent patterns in plane Couette flow [Prigent et al., 2003]. We next quantify the rate of this decrease with Reynolds number using a fit of the form $\sim O(Re^\alpha)$. The results in Fig. 3(c)

show that $k_x^M \sim Re^{-0.41}$ and $k_z^M \sim Re^{-0.34}$, indicating a difference in the declination rate of the streamwise and spanwise wavenumbers as Re increases. These trends further support the notion that the inclination angle decreases as a function of the Reynolds number over this range.

4. Reynolds number scaling

In this section, we examine the Reynolds number scalings of the maximal values of the structured and unstructured frequency responses as a function of η. For a given Reynolds number, these maximal frequency responses over spatial wavenumber domain (k_x, k_z) can be respectively quantified as

$$\|\mathcal{H}_\nabla\|_\mu^M := \max_{k_x,k_z} \|\mathcal{H}_\nabla\|_\mu(k_x, k_z), \tag{14a}$$

$$\|\mathcal{H}_\nabla\|_\infty^M := \max_{k_x,k_z} \|\mathcal{H}_\nabla\|_\infty(k_x, k_z), \tag{14b}$$

$$\|\mathcal{H}\|_\infty^M := \max_{k_x,k_z} \|\mathcal{H}\|_\infty(k_x, k_z). \tag{14c}$$

Fig. 4(a) plots these quantities for $Re \in [300, 20000]$, where we again obtain their respective Reynolds number scalings through a fit to $O(Re^\alpha)$. The results reveal that both $\|\mathcal{H}_\nabla\|_\infty^M$ and $\|\mathcal{H}\|_\infty^M$ scale as Re^2, the same scaling seen in both plane Couette and plane Poiseuille flows, see e.g. Trefethen et al. [1993], Jovanović [2004]. However, $\|\mathcal{H}_\nabla\|_\mu^M \sim Re^{1.3}$, and this lower scaling exponent versus the unstructured response is similar to previous results that showed $\|\mathcal{H}_\nabla\|_\mu^M \sim Re^{1.1}$ for plane Couette flow (with laminar profile $U(y) = y$) corresponding to $\eta = -1$ and $\|\mathcal{H}_\nabla\|_\mu^M \sim Re^{1.5}$ for plane Poiseuille flow (with laminar profile) $U(y) = 1 - y^2$ corresponding to $\eta = 1$ [Liu and Gayme, 2021]. This lower amplification of the structured response is consistent with previous observations that the structured feedback weakens the amplification of the lift-up mechanism in a manner similar to that of nonlinear effects in plane Couette and plane Poiseuille flows [Liu and Gayme, 2021].

We next explore how the scaling and structural features vary as a function of η. Fig. 4(b) shows the scaling exponents of the maximal structured frequency response $\|\mathcal{H}_\nabla\|_\mu^M \sim Re^{\alpha(\eta)}$ with laminar profiles defined by equation (1) with $\eta = [-1, 1]$ computed at steps of 0.1 over the Reynolds number range $Re \in [300, 4000]$. Here, the range of Reynolds numbers $Re \in [300, 4000]$ is smaller than previous ones to avoid unstable modes, which correspond to infinite frequency responses. These results indicate that α grows from 1.1 to 1.35 as η increases roughly from -1 to 0.3 and then declines at a low rate

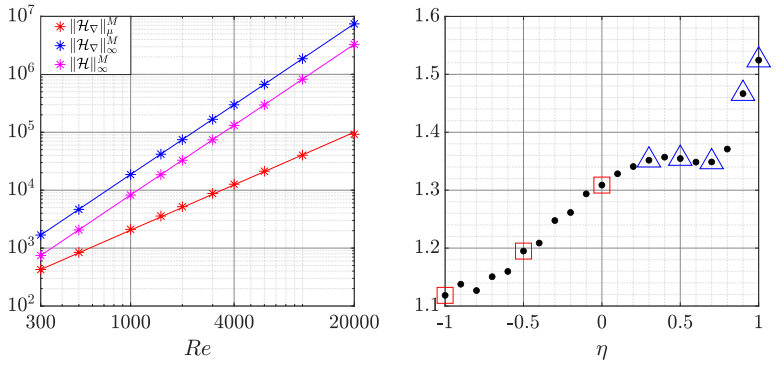

Figure 4: (a) Reynolds number dependence of the maximal structured and unstructured frequency response for $Re \in [300, 20000]$ and $\eta = 0$. Fitted trends indicate $\|\mathcal{H}_\nabla\|_\mu^M \sim Re^{1.3}$, $\|\mathcal{H}_\nabla\|_\infty^M \sim Re^2$ and $\|\mathcal{H}\|_\infty^M \sim Re^2$. (b) The dependence of the scaling exponent α in $\|\mathcal{H}_\nabla\|_\mu^M \sim Re^\alpha$ on the parameter $\eta \in [-1, 1]$ with the range of Reynolds numbers $Re \in [300, 4000]$ which determines the shape of laminar base flow $U(y) = \frac{3(1+\eta)}{4}(y^2 - 1) + \frac{1-\eta}{2}(y - 1) + 1$. The data points marked with red squares (□) in panel are obtained at $\eta = -1, -0.5, 0$, while those with blue triangles (Δ) are at $\eta = 0.3, 0.5, 0.7, 0.9, 1$.

in the range $0.3 \leq \eta \leq 0.7$, before finally climbing to $\alpha = 1.5$ at $\eta = 1$. In contrast, the scalings of both $\|\mathcal{H}_\nabla\|_\infty^M$ and $\|\mathcal{H}\|_\infty^M$ are Re^2 for all $\eta \in [-1, 1]$ (note: since the value remains constant, the corresponding points are not included in Fig. 4(b)). Related scalings of the minimal amplitude of external perturbations that can trigger transition have previously been derived based on simulations [Reddy et al., 1998] and asymptotic analysis [Chapman, 2002] for the special cases of plane Couette ($\eta = -1$) and plane Poiseuille ($\eta = 1$) flow. The analysis based on DNS data predicted minimal perturbation amplitudes of $O(Re^{-1.25})$ for plane Couette flow and $O(Re^{-1.75})$ for Poiseuille flow, while the asymptotic analysis of Chapman [2002] derived respective scalings of $O(Re^{-1})$ and $O(Re^{-1.25})$. A similar Reynolds number scaling of transition-inducing perturbations can be computed from our results as the reciprocal of the structured input-output response using the small gain theorem (provided in Appendix A). The resulting scalings of $O(Re^{-1.1})$ for plane Couette flow and $O(Re^{-1.5})$ for plane Poiseuille flow lie with the range of the scalings predicted using DNS data and asymptotic analysis. The corresponding scalings of transition-inducing perturbations associated with $\|\mathcal{H}_\nabla\|_\infty^M$ and $\|\mathcal{H}\|_\infty^M$ obtained using a similar small gain theorem based analysis is $O(Re^{-2})$ for both

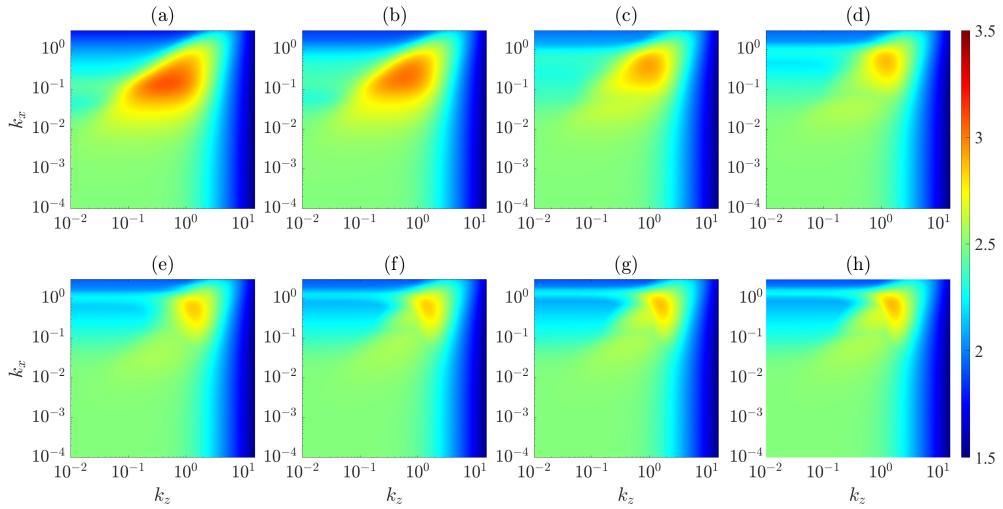

Figure 5: Plots of $\log_{10}[\|\mathcal{H}_\nabla\|_\mu(k_x, k_z)]$ at $Re = 500$ with (a) $\eta = -1$, (b) $\eta = -0.5$, (c) $\eta = 0$, (d) $\eta = 0.3$, (e) $\eta = 0.5$, (f) $\eta = 0.7$, (g) $\eta = 0.9$, and (h) $\eta = 1$. The shape of laminar flow η associated with panels (a)–(c) correspond to the black dots marked with red squares while panels (d)–(h) match with the dots with blue triangles in Fig. 4(b).

flow configurations. This scaling exponent is outside the range predicted by DNS and asymptotic analysis for both flows. It also remains the same for both Couette and Poiseuille flow, which is not consistent with physical arguments in previous work Chapman [2002].

While the scalings of structured responses at $\eta = \pm 1$ are consistent with previous scalings associated with plane Couette and Poiseuille flow, the non-monotonic growth of the scaling exponent was unexpected. In order to analyze thistrend, we examine the structural features associated with the different regimes by computing $\|\mathcal{H}_\nabla\|_\mu(k_x, k_z)$ for laminar profiles with $\eta = -1, -0.5, 0, 0.3, 0.5, 0.7, 0.9$, and 1 at $Re = 500$, which are shown in Fig. 5. Panels (a) – (c) indicate that there is a single peak frequency response region $(k_x, k_z) \approx (10^{-1}, 1)$ associated with oblique flow structures when $-1 \leq \eta \leq 0$. In this region, the scaling increases at a roughly constant rate, and the angle associated with these structures appears to also grow with η. Fig. 4(b) and Figs. 5(d)-(h) indicate that as the base flow becomes more pressure-driven, i.e., in the range $0.3 \leq \eta \leq 0.7$, a new wavenumber region $(k_x, k_z) \approx (1, 0)$ corresponding to a Tollmien-Schlichting (TS) response emerges, and the scaling stops increasing. Given that the laminar flow is no

longer linearly stable for all Reynolds numbers for $\eta > 0.309$ [Balakumar, 1997], these are likely associated with the TS waves that become unstable at higher Reynolds numbers. This TS-wave related peak becomes sharper for $\eta > 0.7$. In addition, the shape of the peak response region associated with the dominant oblique pattern changes for $\eta > 0.7$. This change in flow structure may be associated with the change in Re scaling observed in Fig. 4(b).

5. Response modes associated with the oblique turbulent bands

We next compute structured response modes and use them to explore the features of the most amplified flow structures. In general, the response modes associated with $\mathbf{H}_\nabla$ can be obtained from a singular value decomposition (SVD) of the discretized frequency response operator, see, e.g., chapter 8 in Jovanović [2004] for details. In this work, we adapt this idea to compute the response modes of associated with the feedback interconnection of $\mathbf{H}_\nabla$ and the block-diagonal uncertainty $\widehat{\boldsymbol{u}}_\Xi$, which represents the gain in our model of the nonlinearity. To this end, we perform the structured singular value decomposition (see Definition B.2 in Appendix B) to obtain

$$\mathbf{D}_L^{upp}\mathbf{H}_\nabla(\mathbf{D}_R^{upp})^{-1} = \mathbf{\Phi}\mathbf{\Sigma}\mathbf{\Psi}^*,$$

and extract the column vectors $\phi_n (n = 1, 2, ..., 9N_y)$ of the matrix $\mathbf{\Phi}$. Here, $\mathbf{D}_L^{upp}$ and $\mathbf{D}_R^{upp}$ are the scaling matrices of $\mathbf{H}_\nabla$, see Definition B.1 in Appendix B.

The column vectors $\phi_n (n = 1, 2, ..., 9N_y)$ are the left structured singular vectors of $\mathbf{H}_\nabla$, i.e., those associated with the vectorized velocity gradients $[(\widehat{\boldsymbol{\nabla}}\widehat{u})^{\mathrm{T}}, (\widehat{\boldsymbol{\nabla}}\widehat{v})^{\mathrm{T}}, (\widehat{\boldsymbol{\nabla}}\widehat{w})^{\mathrm{T}}]^{\mathrm{T}}$. Noting that $\widehat{\boldsymbol{\nabla}}\widehat{u} = [\mathrm{i}k_x\widehat{u}, d\widehat{u}/dy, \mathrm{i}k_z\widehat{u}]^{\mathrm{T}} \in \mathbb{C}^{3N_y}$, we can extract the wall-normally varying structured singular modes of the velocity fluctuations $\widehat{u}$ (along with $\widehat{v}$ and $\widehat{w}$ similarly) from the elements of ϕ_n as:

$$\begin{aligned}
\widehat{u}_n(y) &= [\phi_{n,1}, \phi_{n,2}, ..., \phi_{n,N_y}]^{\mathrm{T}}/(\mathrm{i}k_x) \in \mathbb{C}^{N_y}, \\
\widehat{v}_n(y) &= [\phi_{n,3N_y+1}, \phi_{n,3N_y+2}, ..., \phi_{n,4N_y}]^{\mathrm{T}}/(\mathrm{i}k_x) \in \mathbb{C}^{N_y}, \\
\widehat{w}_n(y) &= [\phi_{n,6N_y+1}, \phi_{n,6N_y+2}, ..., \phi_{n,7N_y}]^{\mathrm{T}}/(\mathrm{i}k_x) \in \mathbb{C}^{N_y}, \\
n &= 1, 2, ..., 9N_y,
\end{aligned} \tag{15}$$

where $\phi_{n,j}$ is the j^{th} element of ϕ_n; i.e., $\phi_n := [\phi_{n,1}, \phi_{n,2}, ..., \phi_{n,9N_y}]^{\mathrm{T}}$. In the following context, we will focus on the primary response modes, i.e., $\widehat{u}_1(y)$,

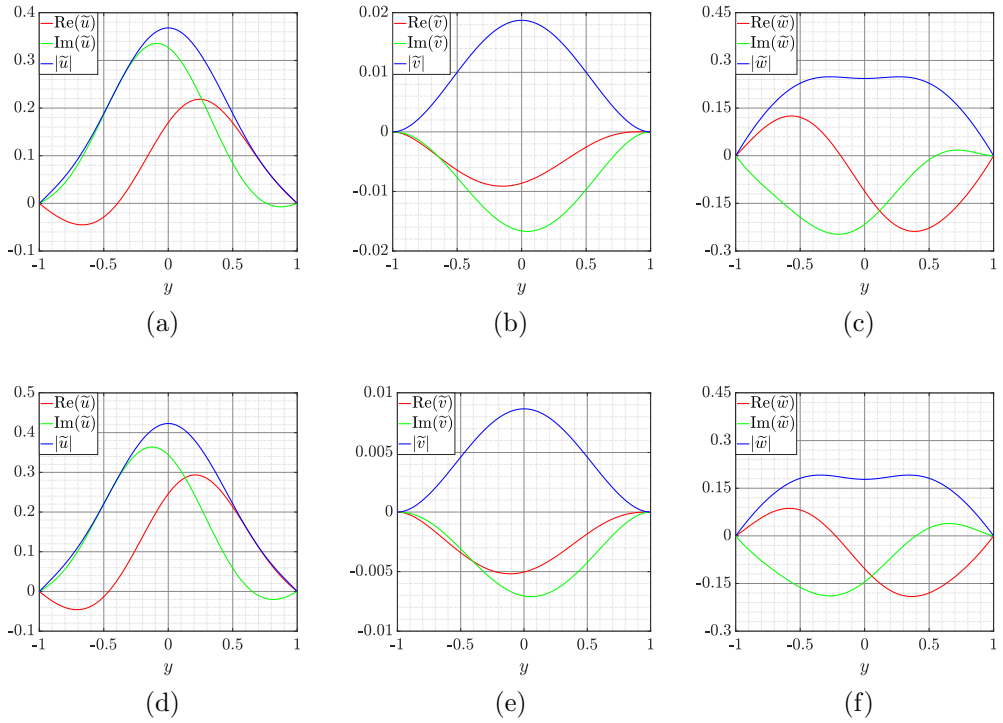

Figure 6: (a)-(c) Primary wall-normal modes $\widehat{u}_1$, $\widehat{v}_1$ and $\widehat{w}_1$ of velocity fluctuations that are obtained using structured singular value decomposition. (d)-(f) Primary velocity modes $\widetilde{u}_1$, $\widetilde{v}_1$ and $\widetilde{w}_1$ obtained from (unstructured) singular vectors of $\mathbf{H}_\nabla$. Both groups of singular vectors correspond to the oblique laminar-turbulent pattern with the triplet $(k_x, k_z, \omega) = (0.0675, 0.1422, 0)$ in plane Couette flow at $Re = 350$ [Chantry et al., 2016]. The red (—), green (—) and blue solid lines (—) represent the real, imaginary part and magnitude of these modes as functions of the wall-normal coordinate, y.

$\widehat{v}_1(y)$ and $\widehat{w}_1(y)$, since they are associated with the largest singular value of the frequency response operator. We also obtain the primary velocity modes without scaling the frequency response operator to show the difference between structured and unstructured response modes. The unstructured response modes are computed following the same procedure described above in eqs.(B.4) and (15), expect that $\mathbf{D}_L^{upp}\mathbf{H}_\nabla(\mathbf{D}_R^{upp})^{-1}$ is replaced by $\mathbf{H}_\nabla$. The corresponding unscaled primary modes are denoted as $\widetilde{u}_1(y)$, $\widetilde{v}_1(y)$ and $\widetilde{w}_1(y)$.

Fig. 6 shows the wall-normal profiles of the structured (in panels (a)-(c)) and unstructured (in panels (d)-(f)) primary velocity modes at $Re = 350$ and $\eta = -1$. This base flow corresponds to the plane Couette flow $U(y) = y$ case studied using DNS in Chantry et al. [2016]. That work focused on the

wall-normal structures of an oblique turbulent band with $k_x \approx 0.0675$ and $k_z \approx 0.1422$, and we those values here for direct comparison. Since we have no data describing the temporal frequency of this flow structure, we estimate ω by computing $\arg\max_{\omega\in\mathbb{R}} \mu_{\widehat{\boldsymbol{U}}_\Xi}[\mathbf{H}_\nabla(k_x,k_z,\omega)]$ and $\arg\max_{\omega\in\mathbb{R}} \bar{\sigma}[\mathbf{H}_\nabla(k_x,k_z,\omega)]$, which leads to $\omega = 0$ in both cases. Fig. 6 shows that both the structured and unstructured singular modes associated with this wavenumber triplet reach their maximal amplitude close to the channel center $y = 0$, meaning that the bulk region of the turbulent band has approximately zero traveling speed. This behavior is consistent with previous findings, which indicate that laminar-turbulent patterns advect at speeds close to that of the bulk velocity $\bar{U}$ at the location where this velocity approaches that of the laminar velocity $U(y)$ [Fukudome and Iida, 2012]. We note that the structured and unstructured singular modes of the same velocity component are identical in shape but differ in their relative magnitudes. This similarity suggests that both methods perform similarly in capturing the wall-normal variation of primary singular modes of the three velocity components for the particular wavenumber pair of interest.

We next use the singular vectors to reconstruct the velocity fluctuations $u(x,y,z,t), v(x,y,z,t)$ and $w(x,y,z,t)$ following the approach in Moarref et al. [2013] which ensures the resulting structures satisfy the incompressibility condition. These fluctuations are given by

$$u(x,y,z,t) = \sum_{n=1}^{3N_y} \sigma_n \cos(k_z z)\mathrm{Re}(\widehat{u}_n(y;k_x,k_z,\omega)e^{\mathrm{i}(k_x x-\omega t)}), \tag{16a}$$

$$v(x,y,z,t) = \sum_{n=1}^{3N_y} \sigma_n \cos(k_z z)\mathrm{Re}(\widehat{v}_n(y;k_x,k_z,\omega)e^{\mathrm{i}(k_x x-\omega t)}), \tag{16b}$$

$$w(x,y,z,t) = -\sum_{n=1}^{3N_y} \sigma_n \sin(k_z z)\mathrm{Im}(\widehat{w}_n(y;k_x,k_z,\omega)e^{\mathrm{i}(k_x x-\omega t)}), \tag{16c}$$

where Re and Im represent the real and imaginary part of the argument $(\cdot)$, respectively. σ_n is the n_{th} singular value of $\mathbf{D}_L^{upp}\mathbf{H}_\nabla(\mathbf{D}_R^{upp})^{-1}$, and $\widehat{u}_n$, $\widehat{v}_n$, and $\widehat{w}_n$ are obtained from the n_{th} structured singular vector ϕ_n (see eq.(15)). Since the largest singular value of the scaled frequency response matrix is much larger than the others, it is reasonable to use only the associated modes $\widehat{u}_1$, $\widehat{v}_1$ and $\widehat{w}_1$ to approximate the large-scale characteristics of the velocity fluctuations corresponding to the oblique flow patterns with $(k_x,k_z,\omega) =$

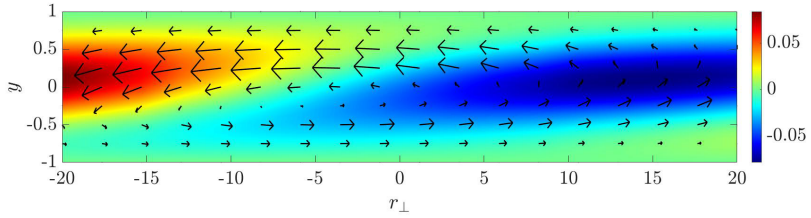

(a)

Figure 7: Reconstruction of the large-scale velocity fluctuations for the same oblique turbulent band as in Fig. 6 based on structured response modes. This two-dimensional slice represents the $r_\perp - y$ plane across the center of turbulent band region. The black arrows ($\rightarrow$) mark two velocity components $(u_\perp, u_y)$, while the background contour shows $u_\parallel$ parallel to the direction of the band, with positive value (red region) indicating that the projection of the three-dimensional velocity in this direction points to the downstream side.

$(0.0675, 0.1422, 0)$.

Fig. 7 shows our reproduction of the velocity field corresponding to the wavenumbers associated with the oblique turbulent bands studied in [Chantry et al., 2016] using the structured response modes. Since the optimal response corresponds to $\omega = 0$, our reconstructed velocity fluctuations are time-invariant and thus can be interpreted as time-averaged velocity fields associated with this oblique band. To compare our prediction of velocity fluctuations with the numerical results in Chantry et al. [2016] that are computed in the tilted domain, we convert our spatial coordinate framework (x, y, z) to $(r_\perp, y, r_\parallel)$, where $r_\perp$ is the coordinate perpendicular to the direction of the oblique turbulent band and $r_\parallel$ is associated with the direction along the band. The velocity components in this new framework are given by

$$u_\perp := -\sin(\theta)u + \cos(\theta)w, \tag{17a}$$

$$u_\parallel := \cos(\theta)u + \sin(\theta)w, \tag{17b}$$

where $\theta \approx 25.4^\circ$ is the inclination angle of the turbulent band according to Chantry et al. [2016]. Compared to the velocity fields in Fig. 3(a) of Chantry et al. [2016], our results in Fig. 7 reproduce the same circular vortex.

The consistency between our prediction of velocity fluctuations and the DNS data motivates the application of this method to predict the wall-normal structure of the oblique turbulent bands in other wall-bounded flows. First, we study the band in plane Couette-Poiseuille flow at $Re = 610$ with the intermediate laminar profile, i.e., $\eta = 0$ in eq.(1). Since the experiments of this

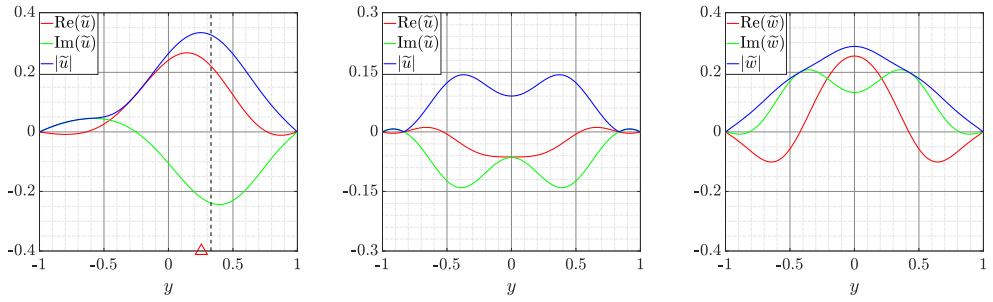

Figure 8: Wall-normal profiles of velocity modes from structured SVD: (a) primary streamwise velocity mode $\widehat{u}_1$ with parameters $(k_x, k_z, \omega) = (0.0676, 0.1309, \approx 0)$ associated with the oblique turbulent band in Klotz et al. [2021]. The black dashed line (- -) at the wall-normal location $y = 0.33$ marks the point of the strongest transient growth [Klotz and Wesfreid, 2017]. The red triangle (Δ) at $y = 0.3285$ marks the maximal amplitude point of the velocity mode. (b)-(c) The primary streamwise $\widehat{u}_1$ and spanwise velocity mode $\widehat{w}_1$ with parameters $(k_x, k_z, \omega) = (0.1887, 0.0897, -0.1615)$ associated with oblique turbulent band in plane Poiseuille flow [Song and Xiao, 2020]. The red, green, and blue solid lines again represent the real and imaginary part and the magnitude of velocity modes respectively.

flow in Klotz et al. [2021] have shown that the wavenumbers of the oblique band are $k_x \approx 0.0676$ and $k_z \approx 0.1309$, we use these parameters along with our estimated temporal frequency $\arg\max_{\omega\in\mathbb{R}} \mu_{\widehat{\boldsymbol{U}}_\Xi} [\mathbf{H}_\nabla(k_x, k_z, \omega)] = -0.005 \approx 0$. Fig. 8(a) shows the wall-normal profile of the primary singular mode $\widehat{u}_1$ associated with the streamwise velocity fluctuation. We find that it reaches the maximum when $y = 0.33$ as marked with the red triangle in the figure, which is also the maximal amplitude point (black dashed line) of the streamwise streaks ($k_x = 0$ and $k_z = 1.83$), i.e., where they achieve the strongest transient growth [Klotz and Wesfreid, 2017]. We next estimate the wall-normal structure of the velocity fluctuations in the oblique turbulent bands in plane Poiseuille flow $U(y) = 1 - y^2$ at $Re = 750$, which was investigated by DNS in Song and Xiao [2020]. A comparison of the structured singular modes computed with the mean fluctuations from DNS data (see Fig. 7 in Song and Xiao [2020]) shows that we obtain similar wall-normal variations (i.e., profile shapes). More specifically, the computed wall-normal profile of our primary mode has the same inflectional feature and similar shape to those obtained from the simulation data. This result again indicates that structured input-output analysis is capable of predicting the wall-normal profile of the velocity

fluctuations associated with the oblique turbulent bands.

6. Oblique turbulent band propagation speeds

In order to study the temporal behavior (advection) of the most amplified structures, we estimate their phase speeds using our structured method. We limit the analysis to the case where the temporal frequency $\omega \in \mathbb{R}$, since any time-dependent flow structure can be represented by integrating its Fourier components over real temporal frequencies [Trefethen et al., 1993]. The advection speed u_c of a given oblique flow structure with $(k_x, k_z) \neq 0$ is then estimated using the phase speed $c := -\omega/k_x$ associated with the highest structured response

$$u_c(k_x, k_z) = -\frac{1}{k_x} \arg\max_{\omega \in \mathbb{R}} \mu_{\widehat{\boldsymbol{U}}_\Xi} \left[\mathbf{H}_\nabla(k_x, k_z, \omega) \right], \tag{18}$$

i.e., the phase speed associated with the optimal temporal frequency ω for a given (k_x, k_z) wavenumber pair. In the following discussion, c and u_c are normalized using the characteristic velocity scale, which defines the Reynolds number for each flow configuration.

In order to validate the approach we focus our investigation on the advection speeds of flow patterns in plane Couette and plane Poiseuille flow, which have been previously studied [Fukudome and Iida, 2012, Tuckerman et al., 2014, Lu et al., 2019, Xiao and Song, 2020a]. Table 1 provides a comparison between the advection speeds of the laminar-turbulent patterns (oblique turbulent bands) predicted from our approach with results computed from DNS [Fukudome and Iida, 2012, Tuckerman et al., 2014, Lu et al., 2019, Xiao and Song, 2020a]. The oblique turbulent band wavenumbers (k_x, k_z) reported were extracted from snapshots of DNS results from Lu *et al.*, 2019, Fig. 3 (b); Tuckerman *et al.*, 2014, Fig. 4 (a); Xiao & Song, 2020, Fig. 1 (a), respectively. We note that the laminar profile of plane Poiseuille flow, as well as the definitions of Reynolds number in Xiao and Song [2020a] and Fukudome and Iida [2012] (row 1 and 2 in Table 1) differ from ours in eq.(1). In order to compare with those results, we renormalize the velocity uniformly using the centerline speed of the base flow, U^*_{cen}. Consequently, here the plane Poiseuille flow is redefined as $U(y) = 1 - y^2$, and the Reynolds numbers in these previous studies [Xiao and Song, 2020a, Fukudome and Iida, 2012] are also converted to the value shown in Table 1 according to the definition $Re := U^*_{cen} h/\nu$. The numerical results in Tuckerman et al. [2014] and Lu et al. [2019] (row

Table 1: Advection speeds u_c of laminar-turbulent patterns in plane Couette-Poiseuille flows obtained by predictions of structured and standard input-output analysis. The laminar profiles $U(y)$, Reynolds numbers Re, and wavenumbers (k_x, k_z) of these flow patterns are selected to match comparison cases from the literature. We note that the Reynolds numbers for all cases shown were converted from those in the references to match the Reynolds number definition in this work. The wavenumbers are obtained from Fig. 1(a) in Xiao and Song [2020b], Fig. 2(b) in Fukudome and Iida [2012], Fig. 2(a) in Tuckerman et al. [2014], and Fig. 3(b) in Lu et al. [2019] respectively, while the DNS results predicting u_c are respectively taken from Fig. 1, Fig. 6, Fig. 4, and Fig. 4. of these references

$U(y)$	Re	(k_x, k_z)	Estimations of u_c by structured approach	Estimations by unstructured approach	DNS
$1-y^2$	750	$(0.15, 0.10)$	0.92	0.90	0.85
$1-y^2$	1242	$(0.09, 0.19)$	0.71	0.73	0.68
$\frac{1}{2}-\frac{3}{2}y^2$	1100	$(0.06, 0.14)$	≈ 0	≈ 0	0.07
y	317	$(0.04, 0.05)$	≈ 0	≈ 0	≈ 0

3 and 4 in Table 1) are based on the same characteristic length and velocity scales as our analysis, so their laminar profiles correspond to the cases where $\eta = 1$ and $\eta = -1$ respectively, so we can directly compare to their results by matching the Reynolds numbers. The results in Table 1 indicate that all of the estimated values are within a reasonable error range when compared to these DNS results. This success in predicting the traveling speeds of the given structures indicates that our framework is can be used to estimate the advection speed of different flow structures.

Table 1 also shows the convective velocities predicted using the unstructured frequency response, which is obtained by substituting the largest singular value $\bar{\sigma}[\mathbf{H}_\nabla(k_x, k_z, \omega)]$ in eq. (18). A similar computation was carried out using the frequency response operator $\mathbf{H}(k_x, k_z, \omega)$, which yielded the same results (these repeated values are not shown in Table 1). The convective velocities predicted using the standard input-output approach are within 5% of those obtained using the structured approach proposed herein for the given wavenumbers. This similarity suggests that, for this case, once the wavenumber pair of interest is identified (through, e.g., DNS, experiments, or the SIOA approach), the unstructured and structured spatio-temporal frequency response operators may provide similar estimates of convective velocities. These results are consistent with previous studies showing that the

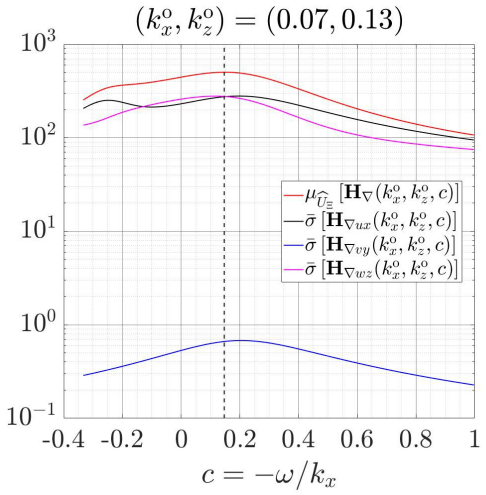

Figure 9: Plots of the structured singular value of discretized frequency response operator $\mu_{\widehat{U}_\Xi}[\mathbf{H}_\nabla]$ (red solid lines —) and the largest unstructured singular values of its three diagonal components $\bar{\sigma}[\mathbf{H}_{\nabla ux}]$ (black —), $\bar{\sigma}[\mathbf{H}_{\nabla vy}]$ (blue —), and $\bar{\sigma}[\mathbf{H}_{\nabla wz}]$ (magenta —). The wavenumbers (k_x^o, k_z^o) belongs to the oblique turbulent band observed in the experiment of plane Couette-Poiseuille flow at $Re = 610$ [Klotz et al., 2021]. The black dashed line representing $c \approx 0.15$ marks the optimal phase speed associated with the largest structured singular value of $\mathbf{H}_\nabla$.

spatio-temporal frequency response operator of the linearized N-S equations can accurately predict convective velocities over a range of length scales, see, e.g., [Liu and Gayme, 2020]. Understanding the similarities in predicting the convective velocity from SIOA and traditional IO across the full range of scales, particularly the smallest scales where nonlinear interactions may play a larger role, is a topic of ongoing work.

The agreement in our prediction using the optimal phase speed c to estimate the advection speed u_c indicates that the structured singular value of the frequency response operator $\mu_{\widehat{\boldsymbol{U}}_\Xi}[\mathbf{H}_\nabla(k_x, k_z, c)]$ is closely related to the optimal phase speed c when the wavenumbers (k_x, k_z) are given. In order to investigate the dependence of μ on the phase speed of a given flow pattern, we again set $Re = 610$ and select the wavenumbers of oblique band $(k_x^o, k_z^o) = (0.07, 0.13)$, based on the values estimated in the of experiments in [Klotz et al., 2021]. We then vary $c = -\omega/k_x$ from $U(y)_{\min} = -0.33$ to $U(y)_{\max} = 1$ and obtain the dependence of structured singular value on the phase speed. The results are shown in Fig. 9 as the red solid line, and indicate that $\mu_{\widehat{U}_\Xi}[\mathbf{H}_\nabla]$ is strongly influenced by c. Moreover, the red solid line has a

notable peak around $c = 0.15$, which suggests that the estimated advection speed of this flow pattern should approximate this value.

We next examine the relationship of this phase speed dependence in the structured versus unstructured singular values of $\mathcal{H}_\nabla$. We start from the following inequality proven in [Liu and Gayme, 2021, equation (3.6)]

$$\|\mathcal{H}_\nabla\|_\mu(k_x, k_z) \geq \max[\|\mathcal{H}_{\nabla ux}\|_\infty, \|\mathcal{H}_{\nabla vy}\|_\infty, \|\mathcal{H}_{\nabla wz}\|_\infty], \tag{19}$$

where

$$\mathcal{H}_{ij} = \widehat{\mathcal{C}}_i(\mathrm{i}\omega\mathcal{I}_{2\times 2} - \mathcal{A})^{-1}\widehat{\mathcal{B}}_j, \tag{20a}$$

$$\mathcal{H}_{\nabla ij} = \widehat{\nabla}\mathcal{H}_{ij}, \quad i = u, v, w, \quad j = x, y, z, \tag{20b}$$

$$\widehat{\mathcal{B}}_x := \widehat{\mathcal{B}}\begin{bmatrix}\mathcal{I} & 0 & 0\end{bmatrix}^{\mathrm{T}}, \widehat{\mathcal{B}}_y := \widehat{\mathcal{B}}\begin{bmatrix}0 & \mathcal{I} & 0\end{bmatrix}^{\mathrm{T}}, \widehat{\mathcal{B}}_z := \widehat{\mathcal{B}}\begin{bmatrix}0 & 0 & \mathcal{I}\end{bmatrix}^{\mathrm{T}}, \tag{20c}$$

$$\widehat{\mathcal{C}}_u := \begin{bmatrix}\mathcal{I} & 0 & 0\end{bmatrix}\widehat{\mathcal{C}}, \quad \widehat{\mathcal{C}}_v := \begin{bmatrix}0 & \mathcal{I} & 0\end{bmatrix}\widehat{\mathcal{C}}, \quad \widehat{\mathcal{C}}_w := \begin{bmatrix}0 & 0 & \mathcal{I}\end{bmatrix}\widehat{\mathcal{C}}. \tag{20d}$$

following the definitions in Jovanović and Bamieh [2005], Liu and Gayme [2021]. This indicates that the structured frequency response is closely related to the unstructured responses associated with the input-output pathways $f_x \to u$, $f_y \to v$, and $f_w \to z$. Such a connection inspires us to compute the corresponding unstructured singular values, i.e., $\bar{\sigma}[\mathbf{H}_{\nabla ux}](k_x, k_z, c)$, $\bar{\sigma}[\mathbf{H}_{\nabla vy}](k_x, k_z, c)$ and $\bar{\sigma}[\mathbf{H}_{\nabla wz}](k_x, k_z, c)$, and compare their dependence on c with that of the structured singular value. Fig. 9 displays these quantities and their variation with phase speed. We first notice that as c varies, we always have the following inequality

$$\begin{aligned}\mu_{\widehat{U}_\Xi}[\mathbf{H}_\nabla](k_x, k_z, c) \geq \max\{&\bar{\sigma}[\mathbf{H}_{\nabla ux}](k_x, k_z, c), \bar{\sigma}[\mathbf{H}_{\nabla vy}](k_x, k_z, c),\\ &\bar{\sigma}[\mathbf{H}_{\nabla wz}](k_x, k_z, c)\}, \forall c \in [U_{\min}, U_{\max}],\end{aligned} \tag{21}$$

for a given (k_x, k_z). This relationship suggests that we may be able to generalize the inequality (19) obtained in Liu and Gayme [2021] from the case of optimal c to any phase speed within the range. In particular, we find that both $\bar{\sigma}[\mathbf{H}_{\nabla ux}]$ and $\bar{\sigma}[\mathbf{H}_{\nabla wz}]$ have similar magnitude and phase speed dependence compared to $\mu_{\widehat{U}_\Xi}[\mathbf{H}_\nabla]$, which indicates a strong correlation between these componentwise unstructured and structured singular values.

7. Conclusions and directions for future Work

In this paper, we apply structured input-output analysis to study transitional plane Couette-Poiseuille flow (CPF). The wavelengths associated with largeest structured response are found to be consistent with the oblique turbulent bands observed in recent experiments with equally weighted components of plane Couette and plane Poiseuille flow in the laminar profile ($\eta = 0$) [Klotz et al., 2021]. As the Reynolds number increases, the most energetic streamwise and spanwise wavenumbers of the oblique patterns associated with the highest structured gain decrease with respective scalings $k_x^M \sim Re^{-0.41}$ and $k_z^M \sim Re^{-0.34}$. The inclination angles of the associated oblique turbulent bands also decline as the Reynolds number increases, consistent with results from experiments of plane Couette flow [Prigent et al., 2003].

The Reynolds number scaling of the maximal structured amplification $\|\mathcal{H}_\nabla\|_\mu^M$ changes non-monotonically as the laminar base profile is varied from plane Couette flow ($\eta = -1$) to plane Poiseuille flow ($\eta = 1$). Our analysis shows that as the pressure gradient contribution to the laminar profile exceeds the limit $\eta \gtrsim 0.3$, another region of large structured frequency response corresponding to the wavenumbers of Tollmien-Schlichting waves emerges, and the scaling exponent decreases slightly.

We then extract the response modes associated with the largest structured response. The wall-normal variation of the oblique modes and corresponding physical structures share similarities with those predicted through DNS [Xiao and Song, 2020b, Chantry et al., 2016].

Finally, we use structured input-output analysis to predict the advection speeds of oblique turbulent bands for plane Couette and plane Poiseuille flow configurations, which are special cases of plane Couette-Poiseuille flow. The results are consistent with DNS observations [Fukudome and Iida, 2012, Tuckerman et al., 2014, Lu et al., 2019, Xiao and Song, 2020b]. We then apply this computation to numerically evaluate the dependence of the structured frequency response on the phase speed. The results enable us to generalize a previously known inequality focusing on the optimal phase speed to allow evaluation at arbitrary phase speeds.

The above results demonstrate the promise of structured input-output analysis of both pressure and shear driven transitional flows between parallel plates. Ongoing work will exploit new tools that enable the computation of structured singular values associated with structured uncertainties in the

form of repeated complex blocks Mushtaq et al. [2022]. Using these tools to extract frequency response modes of the feedback interconnection [Mushtaq et al., 2023], as well as analyzing differences in the obtained optimal perturbations [Liu et al., arXiv:2303.10498], may also enable further insight.

ACKNOWLEDGEMENTS

The authors would like to thank Aishwarya Rath for some helpful comments and discussions of the results. We also gratefully acknowledge partial support from the US National Science Foundation (CBET 1652244). This work was carried out at the Advanced Research Computing at Hopkins (ARCH) core facility (rockfish.jhu.edu), which is supported by the National Science Foundation (NSF) grant number OAC 1920103.

Appendix A. Small gain theorem

In this appendix, we present the small gain theorem, which is used to derived the relationship in (10), see e.g. Zhou et al. [1996], Liu and Gayme [2021] for further details.

Proposition 1 (Small Gain Theorem)**.** *Given* $0 < \beta < +\infty$ *and the wavenumber pair* (k_x, k_z)*. The feedback loop is bounded-input bounded-output stable for all* $\widehat{\boldsymbol{u}}_\Xi \in \widehat{\boldsymbol{U}}_\Xi$ *with* $\|\widehat{\boldsymbol{u}}_\Xi\|_\infty := \sup_{\omega\in\mathbb{R}} \bar{\sigma}[\widehat{\boldsymbol{u}}_\Xi] < \beta^{-1}$ *if and only if:*

$$\|\mathcal{H}_\nabla\|_\mu(k_x, k_z) := \sup_{\omega\in\mathbb{R}} \mu_{\widehat{\boldsymbol{U}}_\Xi}[\mathbf{H}_\nabla(k_x, k_z, \omega)] \leq \beta,$$

where μ *is the structured singular value defined in eq.(10).*

Appendix B. Structured singular value decomposition

In this appendix we provide the definition of scaling matrices associated with the frequency response operator $\mathbf{H}_\nabla$ and the specific process of structured singular value decomposition.

Definition B.1 (Scaling Matrix)**.** Suppose that $\mathbf{H}_\nabla$ is the discretized frequency response operator mapping forcing term to the velocity gradients, we define **scaling matrices** $\mathbf{D}_L^{upp}$ and $\mathbf{D}_R^{upp}$[Packard and Doyle, 1993] as:

$$\mathbf{D}_L^{upp}, \mathbf{D}_R^{upp} := \underset{\mathbf{D}_L, \mathbf{D}_R}{\operatorname{argmin}}\ \bar{\sigma}(\mathbf{D}_L \mathbf{H}_\nabla \mathbf{D}_R^{-1}), \tag{B.1}$$

where

$$\mathbf{D}_L := \text{diag}(d_1\mathbf{I}_{3N_y}, d_2\mathbf{I}_{3N_y}, d_3\mathbf{I}_{3N_y}) \in \mathbb{R}^{9N_y \times 9N_y}, d_1, d_2, d_3 > 0, \tag{B.2a}$$

$$\mathbf{D}_R := \text{diag}(d_1\mathbf{I}_{N_y}, d_2\mathbf{I}_{N_y}, d_3\mathbf{I}_{N_y}) \in \mathbb{R}^{3N_y \times 3N_y}, \tag{B.2b}$$

satisfying

$$\widehat{\mathbf{u}}_\Xi \mathbf{D}_L = \mathbf{D}_R \widehat{\mathbf{u}}_\Xi \tag{B.2c}$$

and $\bar{\sigma}(\cdot)$ represents the largest singular value.

Here, the specific structure of $\mathbf{D}_L$ and $\mathbf{D}_R$ is determined based on our structured uncertainty $\widehat{\boldsymbol{u}}_\Xi$ (see Packard and Doyle [1993]). For this discussion and in the computations we again relax the constraint imposing repeated block structure as discussed in Section 2. The following known relation (see e.g. Young and Doyle [1990], Young et al. [1992], Packard and Doyle [1993])

$$\mu_{\widehat{\boldsymbol{U}}_\Xi}[\mathbf{H}_\nabla] = \mu_{\widehat{\boldsymbol{U}}_\Xi}[\mathbf{D}_L \mathbf{H}_\nabla \mathbf{D}_R^{-1}] \leq \bar{\sigma}[\mathbf{D}_L \mathbf{H}_\nabla \mathbf{D}_R^{-1}], \tag{B.3}$$

indicates that these scaling matrices enable us to approximate μ with its upper bound $\bar{\sigma}$.

In this work, we extract $\mathbf{D}_L^{upp}$ and $\mathbf{D}_R^{upp}$ from the output *VSigma* of the *mussvextract* command in MATLAB[Young et al., 1992]. Then we perform SVD on the scaled frequency response matrix $\mathbf{D}_L^{upp}\mathbf{H}_\nabla(\mathbf{D}_R^{upp})^{-1}$ to obtain singular modes associated with the structured response. The *structured* singular value decomposition is then defined as follows:

Definition B.2 (Structured Singular Value Decomposition)**.** Suppose that $\mathbf{H}_\nabla$ is the frequency response operator mapping structured forcing to the velocity gradients and that $\mathbf{D}_L^{upp}$, $\mathbf{D}_R^{upp}$ are the scaling matrices, then its left and right structured singular vector matrix $\boldsymbol{\Phi}$, $\boldsymbol{\Psi}$ are defined as:

$$\mathbf{D}_L^{upp}\mathbf{H}_\nabla(\mathbf{D}_R^{upp})^{-1} = \boldsymbol{\Phi}\boldsymbol{\Sigma}\boldsymbol{\Psi}^*, \tag{B.4}$$

where

$$\boldsymbol{\Phi} = [\phi_1, ..., \phi_{9N_y}], \phi_i \in \mathbb{C}^{9N_y}, i = 1, 2, ..., 9N_y, \tag{B.5a}$$

$$\boldsymbol{\Psi} = [\psi_1, ..., \psi_{3N_y}], \psi_i \in \mathbb{C}^{3N_y}, i = 1, 2, ..., 3N_y, \tag{B.5b}$$

$$\boldsymbol{\Sigma} = \begin{bmatrix} \boldsymbol{\Sigma}' \\ \mathbf{O}_{6N_y \times 3N_y} \end{bmatrix}, \boldsymbol{\Sigma}' = \text{diag}(\sigma_1, \sigma_2, ..., \sigma_{3N_y}), \sigma_1 \geq \sigma_2 \geq ... \geq \sigma_{3N_y} \tag{B.5c}$$

and $\mathbf{O}$ is the zero matrix, and the asterisk superscript on Ψ represents the conjugate transpose.

References

P. Balakumar. Finite-amplitude equilibrium solutions for plane Poiseuille-Couette flow. *Theor. Comput. Fluid Dyn.*, 9:103–119, 1997.

B. Bamieh and M. Dahleh. Energy amplification in channel flows with stochastic excitation. *Phys. Fluids*, 13:3258–3269, 2001.

M. Chantry, L. S. Tuckerman, and D. Barkley. Turbulent–laminar patterns in shear flows without walls. *J. Fluid Mech.*, 791:R8, 2016.

S. J. Chapman. Subcritical transition in channel flows. *J. Fluid Mech.*, 451: 35–97, 2002.

M. Farano, S. Cherubini, J. C. Robinet, and P. De Palma. Hairpin-like optimal perturbations in plane Poiseuille flow. *J. Fluid Mech.*, 775:R2, 2015.

K. Fukudome and O. Iida. Large-scale flow structure in turbulent Poiseuille flows at low-Reynolds numbers. *J. Fluid Sci. and Technol.*, 7(1):181–195, 2012.

M. R. Jovanović. *Modeling, analysis, and control of spatially distributed systems*. PhD thesis, University of California, Santa Barbara, 2004.

M. R. Jovanović and B. Bamieh. Componentwise energy amplification in channel flows. *J. Fluid Mech.*, 534:145–183, 2005.

T. Kanazawa. *Lifetime and growing process of localized turbulence in plane channel flow*. PhD thesis, Osaka University, 2018.

J. H. Kim, J. H. Hwang, Y. M. Lee, and J. H. Lee. Direct numerical simulation of a turbulent Couette-Poiseuille flow, part 2: Large- and very-large-scale motions. *Int. J. Heat Fluid Flow*, 86:108687, 2020.

L. Klotz and J. E. Wesfreid. Experiments on transient growth of turbulent spots. *J. Fluid Mech.*, 829:R4, 2017.

L. Klotz, A. M. Pavlenko, and J. E. Wesfreid. Experimental measurements in plane Couette-Poiseuille flow: dynamics of the large- and small-scale flow. *J. Fluid Mech.*, 912:A24, 2021.

C. Liu. *Feedback interconnection based input-output analysis of spatio-temporal response in wall-bounded shear flows*. PhD thesis, Johns Hopkins University, 2021.

C. Liu and D. F. Gayme. An input–output based analysis of convective velocity in turbulent channels. *J. Fluid Mech.*, 888:A32, 2020.

C. Liu and D. F. Gayme. Structured input-output analysis of transitional wall-bounded flows. *J. Fluid Mech.*, 927:A25, 2021.

C. Liu, C. P. Caulfield, and D. F. Gayme. Structured input-output analysis of stably stratified plane Couette flow. *J. Fluid Mech.*, 948:A10, 2022.

C. Liu, Y. Shuai, A. Rath, and D. F. Gayme. A structured input-output approach to characterizing optimal perturbations in wall-bounded shear flows. In *American Control Conference (To appear)*, arXiv:2303.10498. URL `https://arxiv.org/abs/2303.10498`.

T. Liu, B. Semin, L. Klotz, R. Godoy-Diana, J.E. Wesfreid, and T. Mullin. Decay of streaks and rolls in plane Couette–Poiseuille flow. *J. Fluid Mech.*, 915:A65, 2021.

J. Lu, J. Tao, W. Zhou, and X. Xiong. Threshold and decay properties of transient isolated turbulent band in plane Couette flow. *Appl. Math. Mech.*, 40:1449–1456, 2019.

R. Moarref, A. S. Sharma, J. A. Tropp, and B. J. McKeon. Model-based scaling of the streamwise energy density in high-Reynolds-number turbulent channels. *J. Fluid Mech.*, 734:275–316, 2013.

T. Mushtaq, D. Bhattacharjee, P. Seiler, and M. S. Hemati. Structured singular value of a repeated complex full block uncertainty. *arXiv:2211.05929*, 2022. URL `https://arxiv.org/abs/2211.05929`.

T. Mushtaq, D. Bhattacharjee, P. Seiler, and M. S. Hemati. Structured input-output tools for modal analysis of a transitional channel flow. In *AIAA SCITECH 2023 Forum*, pages 2023–1805, 2023.

A. Packard and J. Doyle. The complex structured singular value. *Automatica*, 29(1):71–109, 1993.

A. Packard, M.K.H. Fan, and J. Doyle. A power method for the structured singular value. In *Proceedings of the 27th IEEE Conference on Decision and Control*, pages 2132–2137 vol.3, 1988.

A. Prigent, G. Grégoire, H. Chaté, O. Dauchot, and W. van Saarloos. Large-scale finite-wavelength modulation within turbulent shear flows. *Phys. Rev. Lett.*, 89:014501, 2002.

A. Prigent, G. Grégoire, H. Chaté, and O. Dauchot. Long-wavelength modulation of turbulent shear flows. *Physica. D*, 174(1):100–113, 2003.

S. M. E. Rabin, C. P. Caulfield, and R. R. Kerswell. Triggering turbulence efficiently in plane Couette flow. *J. Fluid Mech.*, 712:244–272, 2012.

S. C. Reddy, P. J. Schmid, J. S. Baggett, and D. S. Henningson. On stability of streamwise streaks and transition thresholds in plane channel flows. *J. Fluid Mech.*, 365:269–303, 1998.

T. M. Schneider, J.F. Gibson, and J. Burke. Snakes and ladders: Localized solutions of plane Couette flow. *Phys. Rev. Lett.*, 104(10):104501, 2010.

Y. Shuai, C. Liu, and D. F. Gayme. Structured input-output analysis of oblique turbulent bands in transitional plane Couette-Poiseuille flow. In *Twelfth International Symposium on Turbulence and Shear Flow Phenomena (TSFP12)*. Osaka, Japan, 2022.

B. Song and X. Xiao. Trigger turbulent bands directly at low reynolds numbers in channel flow using a moving-force technique. *J. Fluid Mech.*, 903: A43, 2020.

J. J. Tao, B. Eckhardt, and X. M. Xiong. Extended localized structures and the onset of turbulence in channel flow. *Phys. Rev. Fluids*, 3:011902, 2018.

L. N. Trefethen, A. E. Trefethen, S. C. Reddy, and T. A. Driscoll. Hydrodynamic stability without eigenvalues. *Science*, 261(5121):578–584, 1993.

L. S. Tuckerman and D. Barkley. Patterns and dynamics in transitional plane Couette flow. *Phys. Fluids*, 23(4):041301, 2011.

L. S. Tuckerman, T. Kreilos, H. Schrobsdorff, T. M. Schneider, and J. F. Gibson. Turbulent-laminar patterns in plane Poiseuille flow. *Phys. Fluids*, 26(11):114103, 2014.

L. S. Tuckerman, M. Chantry, and D. Barkley. Patterns in wall-bounded shear flows. *Annu. Rev. Fluid Mech.*, 52(1):343–367, 2020.

J. A. Weideman and S. C. Reddy. A MATLAB differentiation matrix suite. *ACM Trans. Math. Softw.*, 26(4):465–519, 2000.

X. Xiao and B. Song. The growth mechanism of turbulent bands in channel flow at low Reynolds numbers. *J. Fluid Mech.*, 883:R1, 2020a.

X. Xiao and B. Song. Kinematics and dynamics of turbulent bands at low Reynolds numbers in channel flow. *Entropy*, 22(10):1167–1183, 2020b.

P. M. Young and J. C. Doyle. Computation of mu with real and complex uncertainties. In *29th IEEE Conference on Decision and Control*, volume 3, pages 1230–1235, 1990.

P. M. Young, M. P. Newlin, and J. C. Doyle. Practical computation of the mixed μ problem. In *1992 American Control Conference*, pages 2190–2194, 1992.

K. Zhou, J.C. Doyle, and K. Glover. *Robust and Optimal Control*. Prentice Hall, 1996.